

Research Article

Model Test Study on Cylindrical Blasting Stress Wave Propagation across Jointed Rock Mass with Different Initial Stresses

Qian Dong ^{1,2}, XinPing Li ³, and JunHong Huang ⁴

¹Hubei (Wuhan) Institute of Explosion Science and Blasting Technology, Jiangnan University, Wuhan, Hubei 430056, China

²Hubei Key Laboratory of Blasting Engineering, Jiangnan University, Wuhan, Hubei 430056, China

³Hubei Key Laboratory of Road-bridge and Structure Engineering, Wuhan University of Technology, Wuhan, Hubei 430070, China

⁴School of Safety Science and Emergency Management, Wuhan University of Technology, Wuhan, Hubei 430070, China

Correspondence should be addressed to Qian Dong; dongqian@jhun.edu.cn

Received 8 June 2020; Revised 12 July 2020; Accepted 10 August 2020; Published 28 August 2020

Academic Editor: Chunshun Zhang

Copyright © 2020 Qian Dong et al. This is an open access article distributed under the Creative Commons Attribution License, which permits unrestricted use, distribution, and reproduction in any medium, provided the original work is properly cited.

In the drilling and blasting excavation of underground rock mass, the stress wave produced by the blasting holes usually propagates in the form of cylindrical wave, while the rock mass surrounding the underground engineering is initially subjected to the in situ stress. To explore the propagation and attenuation law of cylindrical stress wave in the in situ stressed rock mass, a model test of cylindrical blasting stress wave propagation across the intact and jointed rock mass under different initial stresses was carried out. First, the attenuation law of the cylindrical stress wave in the intact rock mass under different confining pressures is analysed, and then the influence of the confining pressure scales, the angle, and the number of joints on the propagation law of the cylindrical blast wave in the jointed rock mass is studied. The experimental results show that the physical attenuation of the cylindrical wave in the intact rock mass decreases and then increases as the confining pressure increases from zero. Under zero confining pressure, the transmission coefficient of the cylindrical wave in the jointed rock mass decreases with the increase of joint angle, and the transmission coefficient increases with the increase of the joint angle under confining pressure. As the confining pressure increases from zero, the transmission coefficient shows a trend of increasing firstly and then decreasing.

1. Introduction

Within Earth's crust, the underground rock mass is usually in a certain initial in situ stress environment. In geophysics, earthquake engineering, underground engineering blasting excavation, and rock dynamics, it is of great significance in the research of the propagation and attenuation of blasting stress wave in in situ stressed rock mass.

The natural rock mass contains a large number of joints which have a great impact on the mechanical properties of rock mass and the propagation of stress wave [1–8]. At present, most of the rock mass excavation involved in underground engineering still adopts the drilling and blasting method. The stress wave produced by the blasting holes of

underground explosions is usually assumed to propagate in cylindrical form and to decay in the underground jointed rock mass [9]. Unlike the plane stress wave, the propagation process of cylindrical stress wave in jointed rock mass is more complicated. Chai et al. [10] analysed the propagation process of cylindrical P-wave across an elastic joint and determined the transmission and reflection coefficients at different positions of the joint. Jalali et al. [11] studied the surface vibration of a cylindrical canyon caused by a cylindrical SH wave in an arbitrary orientation.

The underground in situ rock mass during blasting excavation is subjected to complicated loading conditions, which mainly include in situ stress and blasting loading [12]. The presence of in situ stress affects the stress wave

propagation and attenuation [13, 14]. Ahmed and Abo-Dahab [15] investigated the Love wave propagation in an orthotropic material under the influence of initial stress and the gravity field. The existence of initial stress not only affects the propagation of stress wave in rocks but also changes the stress state of joints, thus changing the propagation law of stress wave in jointed rock mass. Fan and Sun [16] used the nonlinear Bandis-Barton (B-B) model to simulate the deformation characteristic of joints and adopted the displacement discontinuity method (DDM) to study seismic wave propagation through an in situ stressed rock mass.

At present, experimental research on the propagation law of stress wave primarily uses the Split Hopkinson Pressure Bar (SHPB) apparatus [17], but most research involves only one-dimensional stress wave [18–22]. Meanwhile, in the experimental study of the stress wave propagation law under initial stress, some scholars have added the confining pressure and axial pressure-loading device to the SHPB system [23], which only relates to the propagation of one-dimensional stress wave under initial stress [24]. Thus, the experimental study of the propagation law of two-dimensional stress wave (cylindrical wave) in jointed rock mass under initial stress is urgently needed.

Therefore, a model test of cylindrical blasting stress wave propagation across the jointed rock mass under different initial stresses is carried out, and the influencing factors, such as the scale of the initial stress, the angle, and the number of joints, are discussed, respectively. In contrast, the propagation of cylindrical stress wave in the intact rock mass under the same loading conditions is also studied. This study is helpful for better understanding stress wave propagation across in situ stressed rock mass and is of considerable importance to the design of the blasting excavation of rock mass in underground engineering.

2. Model Test

2.1. Initial Stress Loading Equipment. The multifunctional testing machine for rock and soil is adopted to provide steady and uniformly distributed static boundary loads in the model test, as shown in Figure 1. Meanwhile, the length, height and thickness of the model test sample are 1600 mm, 1300 mm, and 400 mm, respectively, and the schematic diagram of the static loads applied to the sample during the test is shown in Figure 2, in which σ_v and σ_h represent the vertical and horizontal boundary static loads, and the maximum static load is 5 MPa. The loading mode of the test sample is divided into the vertical (Figure 1) and horizontal method (Figure 3); in order to eliminate the influence of the gravity of the test sample on stress wave propagation, the horizontal loading method is adopted.

2.2. Determination of Physicomechanical Parameters of Similar Model Test Materials. The prototype used in the model test is the underground engineering rock mass excavated by the drilling and blasting method. By referring to the physicomechanical parameters of several typical deep underground engineering rock masses in China [25, 26], the



FIGURE 1: Multifunctional testing machine for rock and soil.

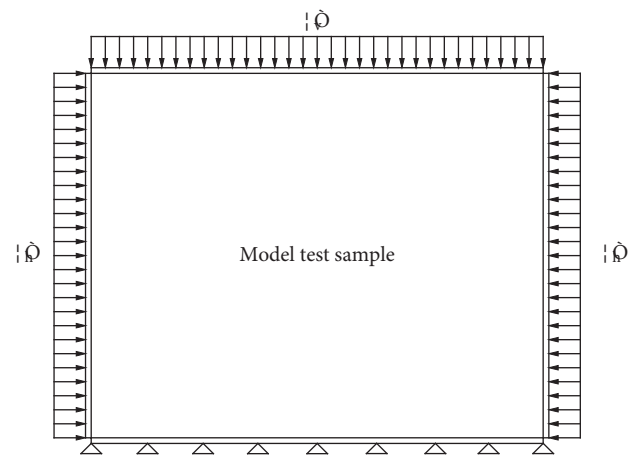


FIGURE 2: The loading diagram for the test sample.



FIGURE 3: Horizontal loading mode.

mechanical parameters of the prototype are comprehensively determined, as shown in Table 1.

The horizontal loading mode is adopted in the model test; that is, the model test samples are placed horizontally, and then static and dynamic loads are applied. Hence, the gravity of the model test samples is borne by the restrained steel girders on both sides of the loading equipment, and the stress similarity coefficient C_σ and the geometric similarity coefficient C_L can be selected independently without

TABLE 1: Physicomechanical parameters of prototype used in the model test.

Type	R_c (MPa)	σ_t (MPa)	E (GPa)	φ (°)	c (MPa)	μ	ρ (kg/m ³)
Prototype	120	12	50	30	30	0.223	2600

R_c , σ_t , E , φ , c , μ , and ρ are the uniaxial compressive strength, tensile strength, elastic modulus, internal friction angle, cohesion, Poisson ratio, and density of the prototype and similar material, respectively.

considering the gravity similarly coefficients C_p [27]. According to the accuracy requirements and test workload of the model test, and by referring to the long-term practical experience of model testing accumulated by the cooperative research group, a stress similarity coefficient C_σ of 20 was selected. Based on the determined stress similarity scale and the physicomechanical parameters of the model test prototype, similar materials can be used as low-strength cement mortar, which is convenient for material acquisition and the manufacture of the model test sample.

In this paper, similar materials are mainly made of cement mortar and supplemented with some additional materials to simulate the intact rock. In the model test, the mixture ratio of the cement mortar in accordance with the similarity theory was determined through the orthogonal test, in which the cement: sand: water: plasticizer ratio = 1 : 4: 1.2:0.0267. Through the following series of tests, the physical and mechanical parameters of the cement mortar material with the chosen mixture ratio are determined.

The uniaxial compressive strength of the similar materials is measured by a uniaxial loading test, as shown in Figure 4. Four φ 50 mm \times 100 mm samples are fabricated, and a set of orthogonal strain gauges are pasted in the middle of the specimen to measure the axial and lateral strains of the specimen during uniaxial loading, respectively.

The typical stress-strain curve is shown in Figure 5, where the abscissa positive and negative values ε_1 and ε_2 are the axial and lateral strain of the sample, respectively, and the ordinate is the applied axial load. The uniaxial compressive strength R_c was 5.732, 5.954, 5.843, and 5.927 MPa, with an average value of 5.864 MPa, and the elastic modulus E_{50} was 5.114, 5.274, 5.254, and 5.262 GPa, with an average value of 5.226 GPa.

At the same time, the Poisson ratio of the model material can be determined by the stress-strain curve of the uniaxial loading test. The Poisson ratios of the model materials were 0.197, 0.209, 0.205, and 0.201, with an average of 0.203.

The tensile strength of the model material is measured by a split test. A total of ten specimens are made, and the size of each specimen is φ 50 mm \times 50 mm; the splitting failure diagram of the specimen is shown in Figure 6. The load P corresponding to the splitting failure of the test specimen is recorded and the tensile strength σ_t can be calculated as

$$\sigma_t = \frac{2P}{\pi DL}, \quad (1)$$

where D and L are the diameter and thickness of the specimen. By using (1), the tensile strength measured could be calculated and was found to be 0.411, 0.568, 0.586, 0.626, 0.724, 0.678, 0.492, 0.586, 0.703, and 0.751 MPa, with an average value of 0.613 MPa, which is the tensile strength of the similar materials.



FIGURE 4: Uniaxial loading test.

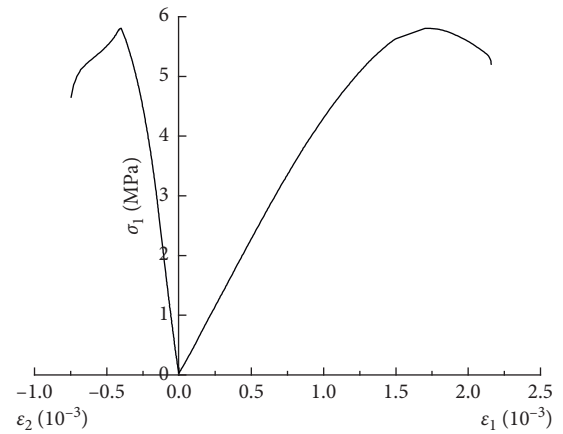


FIGURE 5: Typical stress-strain curves of the test sample under uniaxial compression.

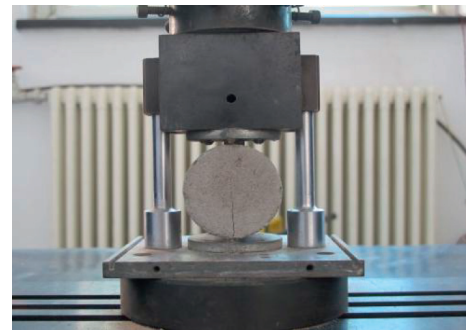


FIGURE 6: Split test.

To measure the internal friction angle and cohesion force of the similar materials, a two-sided shearing test is carried out, and the size of sample is φ 50 mm \times 100 mm. The axial

load is first applied to the sample with a manual hydraulic pump, as shown in Figure 7. After loading the design axial load, the oil pressure is stabilized, and the shearing load is then applied until the specimen is sheared to failure. The critical shear force F_{cr} applied at the moment of shear failure of the specimen is recorded, and the shear strength τ of the similar materials can be obtained by

$$\tau = \frac{F_{cr}}{2\pi r^2}, \quad (2)$$

where r is the radius of the shear test sample.

The axial load applied was 0, 1, 2, 3, and 4 MPa and the two-sided shearing tests at each applied axial load were carried out 4, 3, 3, 4, and 4 times, respectively. The critical shear force F_{cr} under different applied axial loads is recorded, and the change law of the shear strength of the similar materials under different axial stresses is obtained by using (2), as shown in Figure 8.

As shown in the above figure, the shear strength increases with the increase of axial stress. According to the Mohr–Coulomb strength criterion, the relationship between shear strength and axial stress is calculated as

$$\tau = \sigma \tan \phi + c, \quad (3)$$

where c and ϕ are the cohesive force and internal friction angle of the model material, respectively. The shear strength of the model material under different axial stresses in Figure 8 is fitted by (3); the cohesion of the model material is 1.49 MPa, and the internal friction angle is 23.2°.

The physicochemical parameters and stress similarity coefficient C_σ of the similar materials are organized and shown in Table 2. It can be seen that the physical and mechanical parameters of similar materials and the prototype basically satisfy the similarity relationship required by the model test.

2.3. Mechanical Properties of the Joint Simulation Material.

The prototype used in the model test is the underground engineering rock mass subjected to the in situ stress, and the joints in the rock mass are usually in the closure state under compression. Consequently, the joints in the model test samples are also considered as closed joints. To ensure that the joint simulation materials do not deform or break during the manufacturing process of the model test samples, mica plates with certain strength and a thickness of 1 mm are used to simulate the joint in the rock mass. To determine the normal loading mechanical properties of the mica plate, a circular sheet with a diameter of 50 mm and a thickness of 1 mm is fabricated, as shown in Figure 9(a), and then a normal loading test is carried out, as shown in Figure 9(b).

The typical normal stress and deformation curves of the joint simulation materials are shown in Figure 10. It can be seen that the normal stress and deformation of the joint simulation material are in accordance with the nonlinear relationship, and the initial stiffness of the mica plate is 12 GPa/m, which is consistent with the mechanical properties of joints under in situ stress [28].

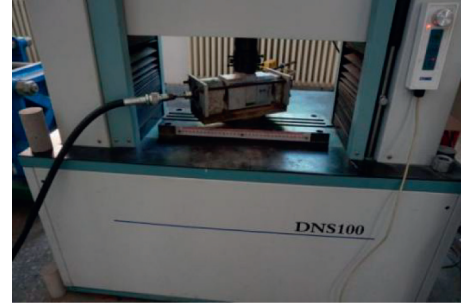


FIGURE 7: Two-sided shearing test.

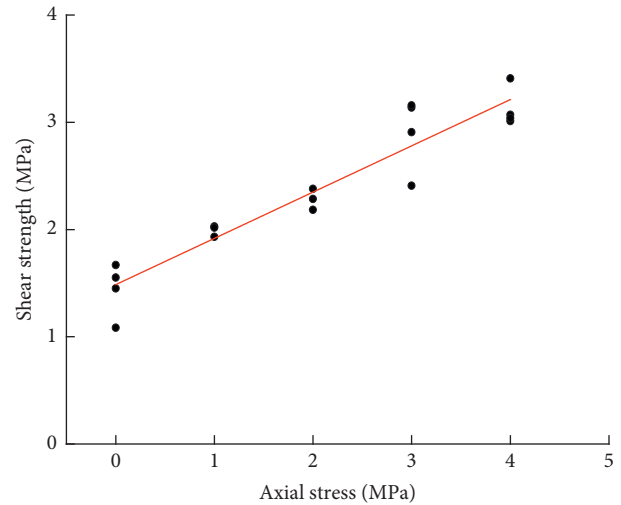


FIGURE 8: Relationship between shear strength and axial stress.

2.4. Design and Manufacture of the Model Test Samples.

The two model test samples were designed as shown in Figure 11 and named T1 and T2. According to the uniformity of the cylindrical wave propagation in all directions, two test sections were arranged in the two model test samples, which are the strain and stress test sections.

In the two samples, four measuring lines are arranged on the strain test section, and four strain measuring points are embedded in each line and numbered from 1 to 16 to measure the radial strain of the model test sample caused by cylindrical stress wave. On the stress test section, two pressure measuring points are arranged on each line and numbered from 17 to 24 to measure the radial stress, which coincides with the projection of the strain measuring point before and after the joint in the thickness direction of the model test samples.

In the T1 and T2 samples, in addition to one measuring line not being arranged on the joints, the other three measuring lines are arranged on 1 or 2 joints, as shown in Figure 11. The angles between the joints and measuring line are 30, 60, and 90 degrees and the length of each joint is 200 mm, which are used to study the propagation and attenuation law of the cylindrical wave in the intact rock mass and the single-joint and double-joint rock masses of 30 degrees, 60 degrees, and 90 degrees, respectively.

TABLE 2: Physicomechanical parameters and stress similarity coefficient of the similar materials.

Type	R_c (MPa)	σ_t (MPa)	E_{50} (GPa)	φ (°)	c (MPa)	μ	ρ (kg/m ³)
Similar material	5.864	0.613	5.226	23.2	1.49	0.203	1980
C_σ	20.5	19.6	9.6	—	20.1	—	—



FIGURE 9: Normal mechanical properties test of the joint simulation material. (a) Circular mica plates. (b) Normal loading test.

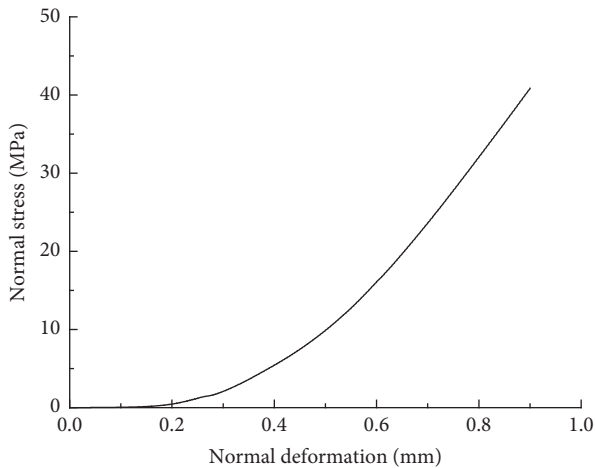


FIGURE 10: Normal stress and deformation curve of the joint simulation material.

To avoid the expansion of joints in the model test samples under the blast load and reduce the influence of the reflected stress wave at joints on different measuring lines affecting the stress wave propagation on other measuring lines, the joint length in the model test samples should not be too large and was set as 200 mm. At the same time, the measuring points arranged before and after the joints in the model test samples are located on the central line of the joints as shown in Figure 11, so it can be approximately considered that when the cylindrical stress wave propagates along the central line of the joints, it is not affected by the scattering of the stress wave at the joint tip.

Before pouring the model test samples, the position of the joint is determined first, and the mica plates are fixed by the homemade device to constrain the displacement during the sample pouring process, as shown in Figure 12.

Both model test samples are divided into 3 layers for pouring, as shown in Figure 13. The thickness of the first

layer is 150 mm and is cured for 1 d; when the layer surface reaches a certain strength, the homemade PVDF (polyvinylidene fluoride) pressure sensors are embedded. Then, the second layer is poured; the thickness of the second layer is 100 mm and resistive strain sensors are embedded on its surface after 1 d of maintenance. Finally, the third layer with a thickness of 150 mm is poured. The model test samples are finished by pouring and after 28 d maintenance, the explosive load can be applied.

To avoid the different cohesion strength between each layer of model test samples during layered pouring, the layered surface of the similar materials is made into a rough surface with a thickness of approximately 5 mm, as shown in Figure 14. Through the above method, the similar materials poured in each layer can be closely combined to ensure the integrity of the model test samples, to reduce the influence of stress wave propagation.

2.5. Test Procedure. Owing to the complicated and high cost of making model test samples, the scheme of repeatedly applying blasting load to single test samples under different scales and distributions of static load is adopted to improve the efficiency of the model test. The cylindrical stress wave applied in the test sample is generated by using an electric detonator to detonate four detonating fuses with a total length of 1.6 m. The TNT (trinitrotoluene) equivalence is approximately 17.6 g, and the charge is kept constant during the test. The main model test steps are as follows.

- (1) The four detonating fuses are tied together and fixed in the seamless steel pipe in the centre of the test sample through the wooden centring stent, as shown in Figure 15. To realize the scheme of repeatedly applying blasting load, the quick-drying materials are poured into the seamless steel tube as the loading core in the model test samples and then maintained for 24 hours, until the strength of the quick-drying material is close to the rock simulation material.

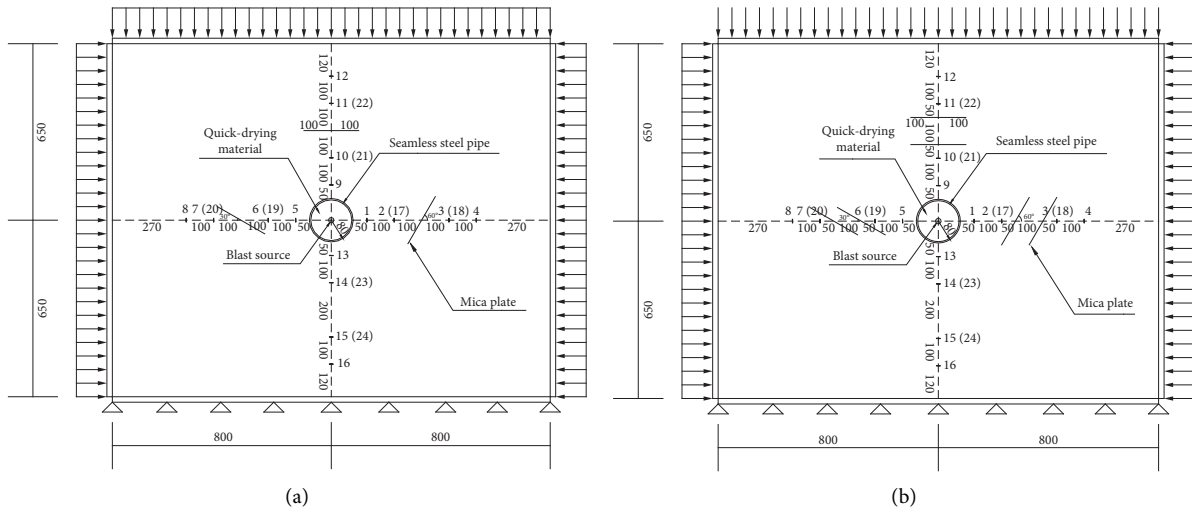


FIGURE 11: Arrangement of measuring points (unit: mm). (a) T1 sample. (b) T2 sample.



FIGURE 12: Layout of the joints in the model test samples. (a) T1 sample. (b) T2 sample.

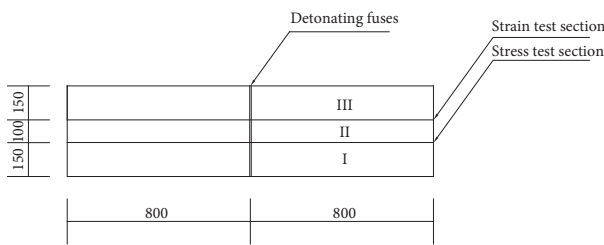


FIGURE 13: Schematic diagram of layered pouring (unit: mm).

- (2) After the model test sample is fixed on the multi-functional testing machine for rock and soil, the preset static load is applied. To facilitate the full deformation of the model test samples, the static loads are divided into two stages and slowly loaded to the design value. The first stage is loaded to one-half of the preset value and lasts for 15 min; the second stage is loaded to the design value and finally stabilized for 30 min.
- (3) Keep the model test samples under a stable static load, and then detonate the detonating fuses. At the

same time, the DH 5960 dynamic data acquisition instrument is used to collect the dynamic stress and strain time-history curve of each measuring point in the model test samples under the blasting load.

- (4) When the dynamic data collection is finished, the three restrained steel beams near the seamless steel tube in the model test samples are removed; then the quick-drying material in the steel pipe is smashed by an electric drill, and removed manually.

After the above four steps are completed, the wooden centring stent with detonating cords can be placed again in the seamless steel tube, and the quick-drying material can be poured. When the strength of quick-drying material reaches the strength required by the model test, the next blasting test can be carried out.

In the model test, the boundary static loads applied to the T1 and T2 samples are the same and are shown in Table 3. The corresponding initial in situ stresses are also shown in Table 3 according to the similarity theory. For each test sample, four different boundary static loads are carried out to study the propagation law of the cylindrical stress wave in the intact and jointed rock mass under different two-dimensional equivalent confining pressures.



FIGURE 14: Surface treatment of similar materials poured in layers. (a) Fabrication of rough surface. (b) Finished rough surface.



FIGURE 15: Schematic diagram of charge structure.

TABLE 3: Boundary static loads of test samples.

Number	Experiment load (MPa)		Initial in situ stress (MPa)	
	Vertical	Horizontal	Vertical	Horizontal
1	0	0	0	0
2	0.75	0.75	15	15
3	1.5	1.5	30	30
4	3	3	60	60

3. Attenuation Law of Cylindrical Wave in Intact Rock Mass under Initial Stress

3.1. Uniformity Analysis of Cylindrical Wave Propagation. To determine whether the propagation of the cylindrical stress wave produced by the detonating fuses in all directions is uniform in the model test samples, the strain measuring points 1, 5, 9, and 13 which are of same distance to the explosion source in the two test samples are taken as the research objects. The strain time-history curves of each measuring point without confining pressure are shown in Figure 16.

The strain peaks of measuring points 1, 5, 9, and 13 in the T1 sample are -228.82×10^{-6} , -225.99×10^{-6} , -233.91×10^{-6} , and -232.03×10^{-6} , respectively. From the strain waveforms shown in Figure 16(a), the variation trend in the strain time-history curve of each measuring point is almost the same before reaching the strain peak, and the peak value is also close.

The strain time-history curves of the strain measuring points 1, 5, 9, and 13 in the T2 sample are shown in

Figure 16(b), and the strain peaks of the measuring points are -221.3×10^{-6} , -226.54×10^{-6} , -217.66×10^{-6} , and -213.61×10^{-6} . The strain time-history curves of each measuring point are almost overlapped before reaching the strain peak. Figure 16 also shows that the propagation of the blasting stress wave in the T1 and T2 samples is uniform in different directions and conforms to the propagation characteristics of the cylindrical wave. Compared to the T1 sample, the strain peak values of each measuring point of the T1 sample are generally small, but the difference is not large. It shows that the explosion loads produced by the same amount of detonating fuses are almost the same in the two test samples.

3.2. Effect of Confining Pressure. The stress and strain measurement points are arranged in the test samples, and the pressure measuring points record the variation of stress wave amplitude value with time, which can directly show the variation law of the amplitude of the cylindrical blast wave. However, due to the limitations of test conditions, only two pressure measuring points are arranged on each measuring line in the test samples, which is not enough to obtain the propagation law of the cylindrical blasting wave. Therefore, the peak values of the four strain measurement points in the intact rock mass measuring line are chosen to study the propagation and attenuation law of the cylindrical stress wave.

Without the initial stress, the strain time-history curves of the radial strain measuring points 13, 14, 15, and 16 in the intact rock mass of the T1 sample are shown in Figure 17. The zero point in the abscissa of the coordinate axis is the moment when the cylindrical wave is spread to measuring point 13. The peak values of the strain curve are -232.03×10^{-6} , -138.62×10^{-6} , 87.75×10^{-6} , and 52.84×10^{-6} , respectively.

It can be seen in the above figure that the peak strain of each measuring point decreases with the increase of the propagation distance of the cylindrical stress wave without initial stress. When the cylindrical stress wave propagates from measuring point 13 to 16, the amplitude of the peak strain is reduced by 77.2%. To facilitate the study, the absolute value of the strain peak value is used to analyse the attenuation of cylindrical stress wave in intact rock mass.

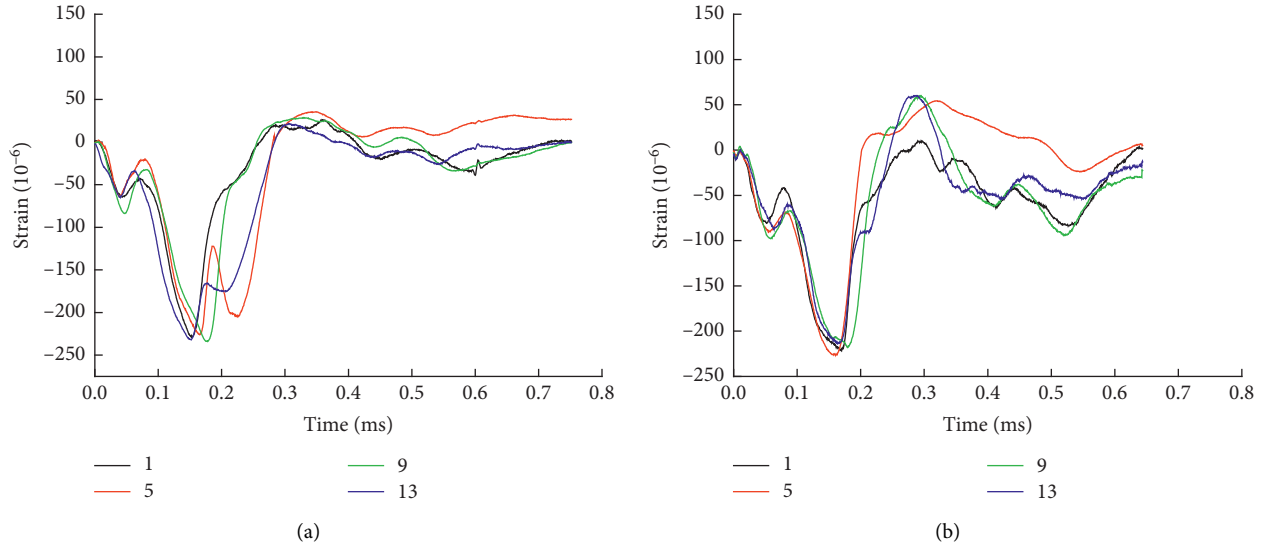


FIGURE 16: Time-history curves of measuring points near explosion source without confining pressure. (a) T1 sample. (b) T2 sample.

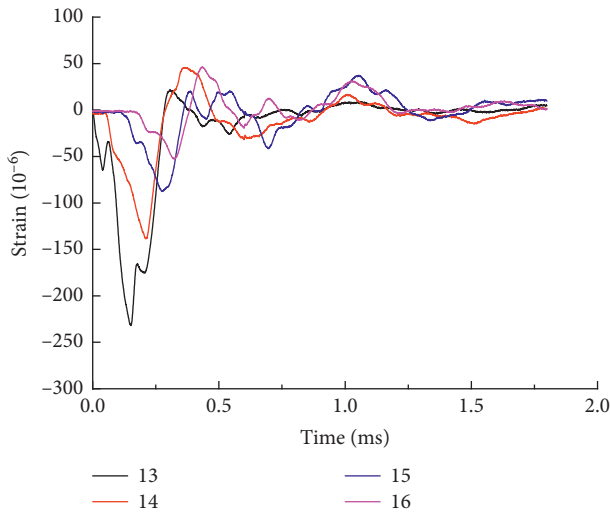


FIGURE 17: Time-history curves of radial strain of measuring point in intact rock mass without initial stress.

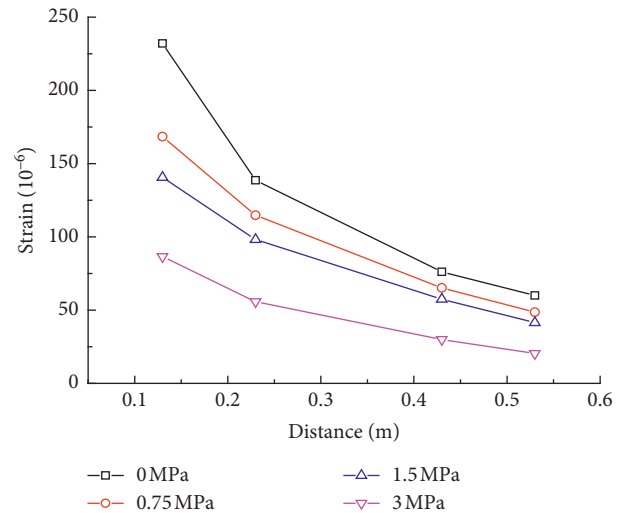


FIGURE 18: Attenuation law of the cylindrical stress wave in the intact rock mass under different confining pressures.

The attenuation law of the strain peak of the measured points in the intact rock mass of the T1 test sample under different confining pressures is shown in Figure 18.

When cylindrical stress wave propagating across intact rock mass, geometric attenuation and physical attenuation both occur as the propagation distance increases. The geometric attenuation is caused by the expansion of the cylindrical stress wave front, which is independent of the physicommechanical properties of the propagating medium and the boundary conditions.

The mechanical parameters of the cylindrical stress wave front are all attenuated by the coefficient $1/\sqrt{r}$ [29], where r is the distance between the wave front and the blasting source. The strain $\varepsilon(r)$ on the wave front is as follows:

$$\varepsilon(r) = \varepsilon_0 \left(\frac{r_0}{r} \right)^{1/2}, \quad (4)$$

where r_0 and ε_0 are the radius and strain of the initial cylindrical stress wave front.

The physical attenuation mechanism of the cylindrical stress wave in the intact rock mass is caused by the friction effect of the stress wave on the microcrack surface inside the propagating medium [30]. The amplitude of the stress wave decreases negatively and exponentially with propagation distance:

$$\varepsilon(r) = \varepsilon_0 e^{-\alpha r}, \quad (5)$$

where α is the physical attenuation coefficient of the cylindrical stress wave.

The physical attenuation of the cylindrical wave in the intact rock mass is affected by the mechanical properties of the propagation medium and the boundary conditions. The geometric attenuation part is eliminated from the attenuation of the peak strain at the measuring points shown in Figure 18 with respect to the propagation distance of the cylindrical wave, and then the physical attenuation law of the cylindrical stress wave in the intact rock mass under different confining pressures is sorted out as shown in Figure 19.

It can be seen in Figure 19 that, with the increase of the cylindrical wave propagation distance, the peak strain of each measuring point decreases, and the greater the confining pressure of the model test block, the lower the strain peak value of the measuring point. It is shown that the larger the static load, the smaller the dynamic response of the intact rock mass.

When the confining pressure increases from 0 to 3 MPa and the cylindrical stress wave propagates from measuring point 13 to measuring point 16, the decreased amplitude of the peak strain is 26.8%, 25.6%, 25.2%, and 30.7%, respectively. It can be seen that the physical attenuation of the cylindrical wave in the intact rock mass decreases first and then increases with the increase of the confining pressure.

The peak strain of the measuring points under different confining pressures in Figure 19 is fitted by (5), which reaches the conclusion that when the confining pressure is increased from 0 to 3 MPa, the physical attenuation coefficients of the cylindrical wave are 0.657, 0.601, 0.586, and 0.749, respectively. Similarly, according to the above method, the physical attenuation coefficients of cylindrical wave in the T2 test sample are 0.641, 0.623, 0.539, and 0.776, respectively. In the two test samples, the variation law of the physical attenuation coefficients of the cylindrical wave propagating across intact rock mass under different confining pressures is summarized in Figure 20.

With the change in confining pressure, the physical attenuation coefficients of the cylindrical wave in the intact rock mass basically meet the cubic function of one variable, as shown in the following:

$$\alpha = 0.0332\sigma^3 - 0.0859\sigma^2 - 0.0036\sigma + 0.649, \quad (6)$$

where σ is the confining pressure and the correlation coefficient is 0.93.

As seen in Figures 19 and 20, the physical attenuation or the physical attenuation coefficient of the cylindrical stress wave propagation in the intact rock mass decreases first and then increases with the increase of the confining pressure.

The reason for this phenomenon is that there are a large number of microcracks inside the intact rock mass, and when the stress wave propagates across the intact rock mass, it will drive the microcracks to slide overcoming the frictional forces. In this process, part of the cylindrical stress wave energy is converted into heat energy, resulting in a decrease in its amplitude. When the confining pressure is low the microcracks in the rock mass are closed, the dynamic stress required for the sliding of the microcracks is also increased, and the number of microcracks that can slip under the stress wave is reduced, so the physical attenuation

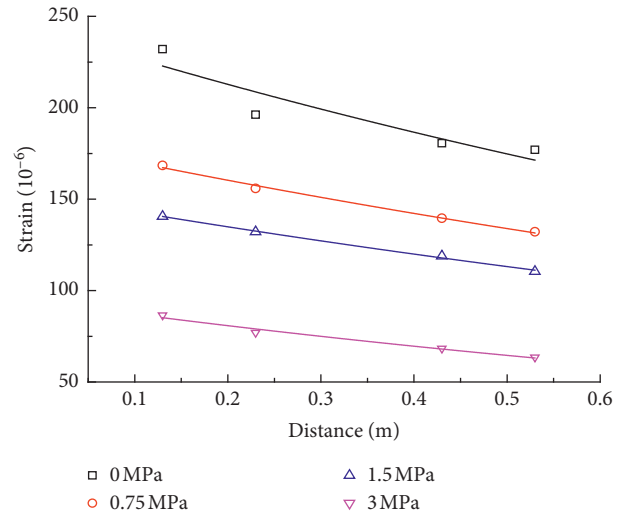


FIGURE 19: Physical attenuation law of cylindrical wave in intact rock mass under different confining pressures.

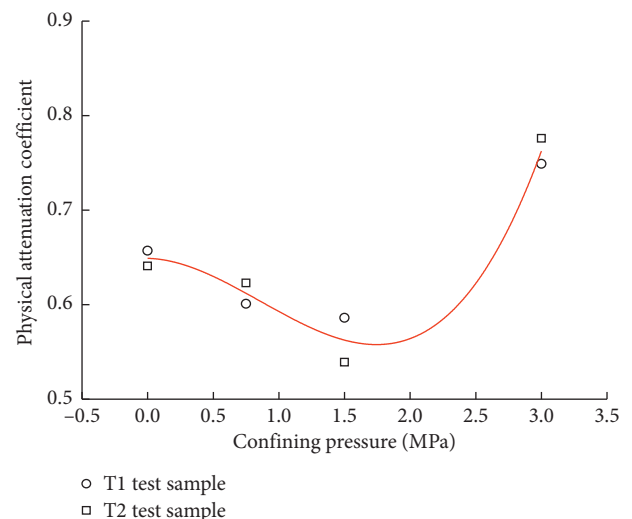


FIGURE 20: Variation law of physical attenuation coefficient under different confining pressures.

of the stress wave decreases. With the increase of confining pressure, the closed microcracks in the intact rock mass are expanded and the new microcracks are initiated, and the number of microcracks that can slip under the stress wave increases, so the attenuation of the stress wave increases accordingly.

4. Propagation Law of Cylindrical Wave in Jointed Rock Mass under Initial Stress

4.1. Effect of Confining Pressure. Because of the existence of joints, the transmission and reflection occur when stress wave passing through the joints will lead to the attenuation of stress wave amplitude. In the absence of confining pressure, the propagation and attenuation law of cylindrical

wave in intact rock mass and 30° single jointed rock masses is shown in Figure 21. There is a discontinuity point when the cylindrical wave propagates through the jointed rock mass, so the propagation and attenuation law of cylindrical wave in jointed rock mass cannot be studied by the same method as the intact rock mass.

Different from the intact rock mass, the ratio of the peak values of the stress measuring points before and after the joints with different angles and numbers in the T1 and T2 samples are taken as the transmission coefficient, to study the propagation law of the cylindrical wave in the jointed rock mass intuitively.

As a comparison, the transmission coefficients of cylindrical wave in intact rock masses are also obtained. The variation law of transmission coefficient of intact and jointed rock mass in T1 and T2 samples under different confining pressures is shown in Figure 22.

It can be seen in Figure 22 that when the confining pressure increases from 0 MPa to 1.5 MPa, the transmission coefficients of jointed rock mass show an increasing trend, and the increased amplitude decreases with the increase of confining pressure. The transmission coefficient of jointed rock mass decreases as the confining pressure increases when confining pressure is greater than 1.5 MPa. For the intact rock mass, with the increase of confining pressure, the transmission coefficient also shows a trend of increasing first and then decreasing, but the amplitude of variation is smaller than that of jointed rock mass. Figure 22 also shows that the larger the confining pressure, the closer the transmission coefficients of the intact and jointed rock masses, which indicates that, with the increase of initial stress, the joints close and gradually lose their effect on the propagation of stress wave.

The reason for the above phenomenon is that the attenuation of the cylindrical stress wave in the jointed rock mass mainly consists of three parts: the physical attenuation resulting from propagation of stress wave in intact rocks, the attenuation resulting from interaction between stress waves and joints, and the geometrical attenuation resulting from the expansion of wave fronts. Meanwhile, it can be seen in Section 3.2 and Figure 20 that the physical attenuation of the cylindrical stress wave in intact rocks of joint rock mass decreases and then increases with the increase of confining pressure, while the geometric attenuation is only related to the geometrical shape of the stress wave front and remains constant in the intact and jointed rock mass. Under the combined action of the cylindrical stress wave and the confining pressure, the joints are nonlinearly deformed, and, with the confining pressure increasing, the stiffness of the joints increases correspondingly, and its attenuation effect on the stress wave is reduced [28].

For the jointed rock mass, when the confining pressure increases from 0 to 1.5 MPa, the attenuation of the cylindrical wave propagating across joints decreases, and the physical attenuation in rocks also reduces, with the result that the attenuation of the cylindrical wave in jointed rock mass decreases, and the transmission coefficient increases. When the confining pressure increases

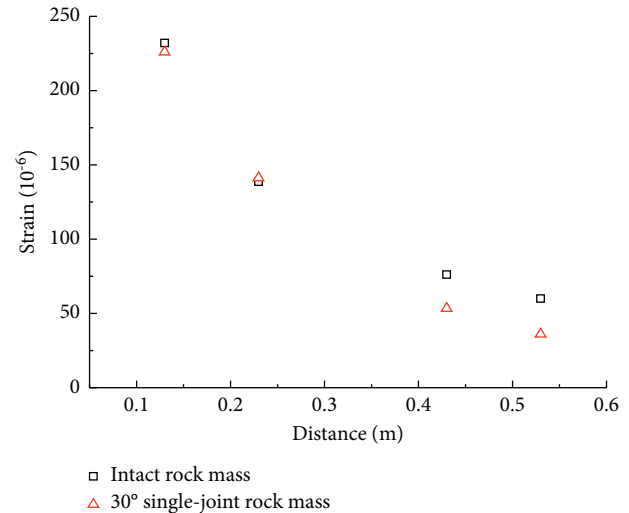


FIGURE 21: Attenuation law of cylindrical wave in the intact and 30° single-joint rock mass without confining pressure.

from 1.5 to 3 MPa, the physical attenuation of cylindrical stress wave in the rocks increases, the attenuation at joints continues to decrease and the transmission coefficients of the jointed rock mass decrease, indicating that the increment of physical attenuation of cylindrical wave in rocks is greater than the decrement of the attenuation at joints.

4.2. Effect of the Number and Angle of Joints. When the confining pressure is 0, 1.5, and 3 MPa, the variation law of the transmission coefficients in jointed rock mass with the angle of joint in T1 and T2 test samples is shown in Figure 23.

Figure 23 shows that the increase of the number of joints will lead to the decrease of transmission coefficients. This is because when the number of joints increases from 1 to 2, in the propagation process of cylindrical stress wave passing through the jointed rock mass, multiple transmission and reflections will occur between the joints, which will lead to the increase of the transmission coefficients to some extent [7]. However, at the same time, amplitude attenuation occurs when cylindrical stress wave passes through each joint. It can be seen from the experimental results that, with the increase of the number of joints, the transmission coefficient decreases, indicating that the attenuation of the cylindrical stress wave at the joint is dominant in the attenuation of the jointed rock mass.

It can also be seen in Figure 23 that when the confining pressure is 0 MPa, the transmission coefficient of the jointed rock mass decreases as the joint angle increases, that is, when the incident angle decreases from 60 to 0 degrees. However, when the confining pressure is greater than 0 MPa, the transmission coefficient increases as the joint angle increases. This is due to the change in the joint angle and generalized normal stiffness of joints under the combined action of confining pressure and cylindrical stress wave.

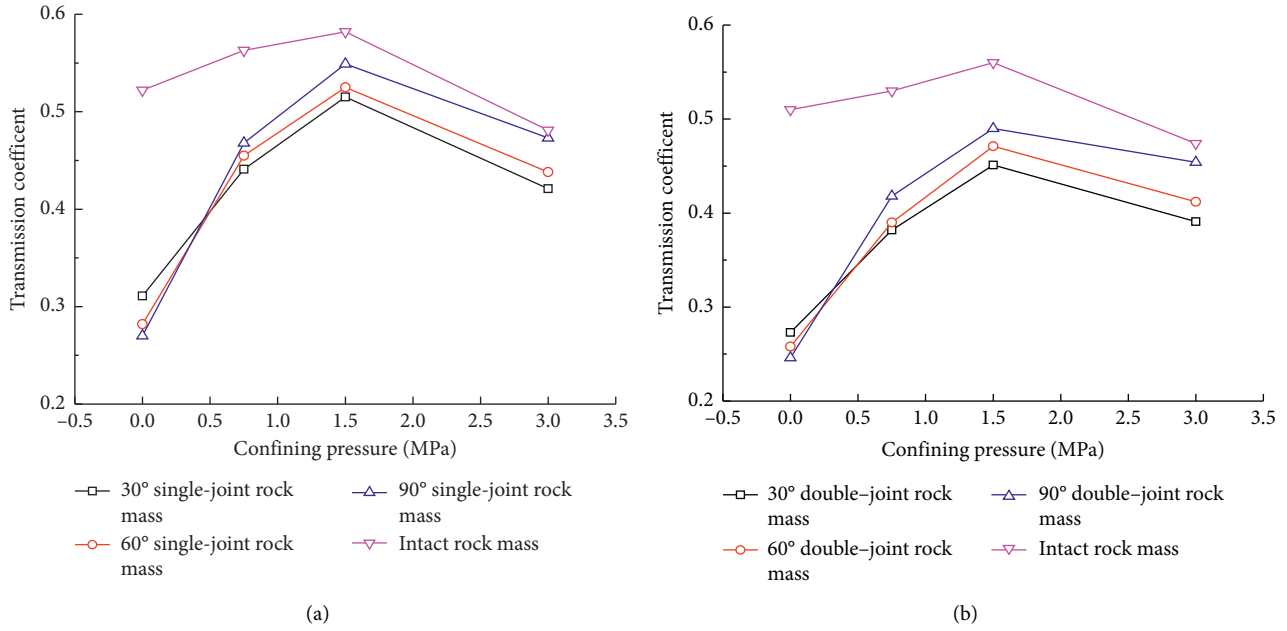


FIGURE 22: Variation law of transmission coefficient of intact and jointed rock mass under different confining pressures. (a) T1. (b) T2.

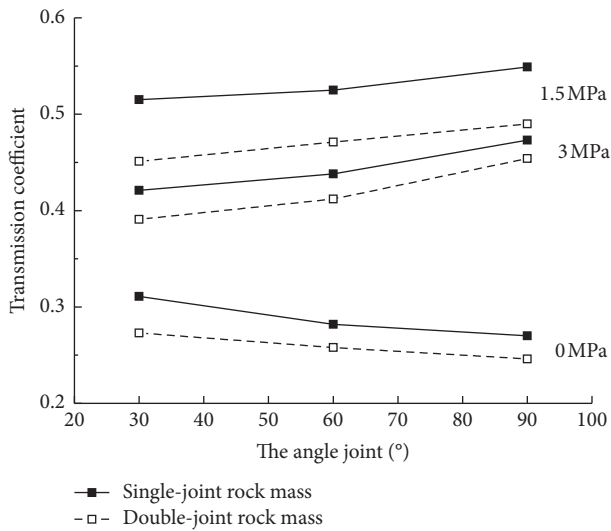


FIGURE 23: Effect of the number and angle of joints on transmission coefficient.

5. Conclusion

According to the propagation characteristics of cylindrical stress wave, the model test samples including the intact rock mass and jointed rock mass were designed, and a model test of cylindrical stress wave propagation under different initial stresses was conducted. Then, through the stress and strain measuring points embedded in different positions of the model samples and the dynamic data acquisition technique, the propagation and attenuation law of the cylindrical wave in the intact and jointed rock mass under initial stress was studied. The model test carried out in this paper can provide a new idea and method for studying the propagation law of

stress wave in jointed rock mass under static loads; moreover, the model test results are helpful for understanding the propagation and attenuation mechanisms of cylindrical stress wave across in situ stressed jointed rock mass. The following conclusions can be drawn:

- (1) The initial stress has a significant impact on the propagation and attenuation of cylindrical stress wave in intact and jointed rock mass, and the rocks and joints of jointed rock mass are in different mechanical states under different initial stresses, which leads to a change in the propagation law of stress wave.
- (2) The attenuation of the cylindrical stress wave in the jointed rock mass mainly consists of three parts: the physical attenuation resulting from the propagation of the stress wave in rocks, the geometrical attenuation resulting from the expansion of the stress wave fronts, and the attenuation resulting from the interaction between stress wave and joints. The geometric attenuation is only related to the geometry of the stress wave front, while the physical attenuation in rocks and the attenuation at the joints are affected by the initial stress.
- (3) For the intact rock mass, a polynomial function can be used to describe the relationship between the confining pressure and the physical attenuation coefficient. With the increase of the confining pressure, the physical attenuation of the cylindrical wave decreases first and then increases.
- (4) The transmission coefficients of the cylindrical wave in jointed rock mass are related to joint angles, quantities, and confining pressures. Without the confining pressure, the transmission coefficient

decreases with the increase of the joint angle. When the confining pressure exists, the transmission coefficient increases with the increase of joint angle. With the increase of confining pressure, the transmission coefficient shows a trend of increasing firstly and then decreasing. The transmission coefficient also decreases as the number of joints increases.

Data Availability

The data used to support the findings of this study are available from the corresponding author upon request.

Conflicts of Interest

The authors declare that there are no conflicts of interest.

Acknowledgments

This study was supported by the Natural Science Foundation of Hubei Province, China (2020CFB428), the National Natural Science Foundation of China (51774222), the Research Start-Up Foundation of Jiangnan University (1027-06020001), and the Postdoctoral Innovation Research Post of Hubei Province of China (20201jb001).

References

- [1] R. Cao, R. Yao, J. Meng, Q. Lin, H. Lin, and S. Li, "Failure mechanism of non-persistent jointed rock-like specimens under uniaxial loading: laboratory testing," *International Journal of Rock Mechanics and Mining Sciences*, vol. 132, Article ID 104341, 2020.
- [2] J. Hu, G. Wen, Q. Lin, P. Cao, and S. Li, "Mechanical properties and crack evolution of double-layer composite rock-like specimens with two parallel fissures under uniaxial compression," *Theoretical and Applied Fracture Mechanics*, vol. 108, Article ID 102610, 2020.
- [3] J. Huang, X. L. Liu, J. Zhao et al., "Propagation of stress wave through fully saturated rock joint under undrained conditions and dynamic response characteristics of filling liquid," *Rock Mechanics and Rock Engineering*, vol. 53, no. 8, pp. 3637–3655, 2020.
- [4] J. Li and G. Ma, "Analysis of blast wave interaction with a rock joint," *Rock Mechanics and Rock Engineering*, vol. 43, no. 6, pp. 777–787, 2010.
- [5] X. Liu, G. Han, E. Wang, S. Wang, and K. Nawnit, "Multiscale hierarchical analysis of rock mass and prediction of its mechanical and hydraulic properties," *Journal of Rock Mechanics and Geotechnical Engineering*, vol. 10, no. 4, pp. 694–702, 2018.
- [6] Q. B. Lin, P. Cao, R. H. Cao et al., "Mechanical behavior around double circular openings in a jointed rock mass under uniaxial compression," *Archives of Civil and Mechanical Engineering*, vol. 20, no. 1, p. 19, 2020.
- [7] J. Zhao, X. B. Zhao, and J. G. Cai, "A further study of P-wave attenuation across parallel fractures with linear deformational behaviour," *International Journal of Rock Mechanics and Mining Sciences*, vol. 43, no. 5, pp. 776–788, 2006a.
- [8] J. B. Zhu, T. Q. Zhai, Z. Y. Liao et al., "Low-amplitude wave propagation and attenuation through damaged rock and a classification scheme for rock fracturing degree," *Rock Mechanics and Rock Engineering*, vol. 53, no. 9, pp. 3983–4000, 2020.
- [9] J. C. Li, G. W. Ma, and Y. X. Zhou, "Analytical study of underground explosion-induced ground motion," *Rock Mechanics and Rock Engineering*, vol. 45, no. 6, pp. 1037–1046, 2012.
- [10] S. B. Chai, J. C. Li, and H. B. Li, "Propagation characteristics of cylindrical wave in joint rock masses," *Chinese Journal of Rock Mechanics and Engineering*, vol. 33, no. 3, pp. 523–530, 2014, in Chinese.
- [11] R. S. Jalali, Z. Tokmechi, and M. D. Trifunac, "A note on the surface motion of a semi-cylindrical canyon for incident cylindrical SH waves radiated by a finite fault," *Earthquake Engineering and Engineering Vibration*, vol. 15, no. 3, pp. 445–455, 2016.
- [12] H. Sun, X. L. Liu, and J. B. Zhu, "Correlational fractal characterisation of stress and acoustic emission during coal and rock failure under multilevel dynamic loading," *International Journal of Rock Mechanics and Mining Sciences*, vol. 117, pp. 1–10, 2019.
- [13] A. N. Guz, V. M. Nazarenko, and V. L. Bogdanov, "Combined analysis of fracture under stresses acting along cracks," *Archive of Applied Mechanics*, vol. 83, no. 9, pp. 1273–1293, 2013.
- [14] M. D. Sharma and N. Garg, "Wave velocities in a pre-stressed anisotropic elastic medium," *Journal of Earth System Science*, vol. 115, no. 2, pp. 257–265, 2006.
- [15] S. M. Ahmed and S. M. Abo-Dahab, "Propagation of love wave in an orthotropic granular layer under initial stress overlying semi-infinite granular medium," *Journal of Vibration & Control*, vol. 16, no. 16, pp. 1845–1858, 2010.
- [16] L. F. Fan and H. Y. Sun, "Seismic wave propagation through an in-situ stressed rock mass," *Journal of Applied Geophysics*, vol. 121, no. 1, pp. 13–20, 2015.
- [17] H. Kolsky, "Stress waves in solids," *Journal of Sound and Vibration*, vol. 1, no. 1, pp. 88–110, 1964.
- [18] J. Feng, E. Wang, L. Chen, X. Li, Z. Xu, and G. Li, "Experimental study of the stress effect on attenuation of normally incident P-wave through coal," *Journal of Applied Geophysics*, vol. 132, pp. 25–32, 2016.
- [19] X. Huang, S. Qi, K. Xia, H. Zheng, and B. Zheng, "Propagation of high amplitude stress waves through a filled artificial joint: an experimental study," *Journal of Applied Geophysics*, vol. 130, pp. 1–7, 2016.
- [20] Y. Ju, L. Sudak, and H. Sudak, "Study on stress wave propagation in fractured rocks with fractal joint surfaces," *International Journal of Solids and Structures*, vol. 44, no. 13, pp. 4256–4271, 2007.
- [21] J. C. Li, N. N. Li, H. B. Li et al., "An SHPB test study on wave propagation across rock masses with different contact area ratios of joint," *International Journal of Impact Engineering*, vol. 105, pp. 109–116, 2016.
- [22] J. C. Li and G. W. Ma, "Experimental study of stress wave propagation across a filled rock joint," *International Journal of Rock Mechanics and Mining Sciences*, vol. 46, no. 3, pp. 471–478, 2009.
- [23] X. Li, Z. Zhou, T.-S. Lok, L. Hong, and T. Yin, "Innovative testing technique of rock subjected to coupled static and dynamic loads," *International Journal of Rock Mechanics and Mining Sciences*, vol. 45, no. 5, pp. 739–748, 2008.
- [24] J. F. Jin, X. B. Li, T. B. Yin et al., "Effect of axial static stress of elastic bar on incident stress wave under axial impact loading," *Engineering Mechanics*, vol. 30, no. 11, pp. 21–27, 2013, in Chinese.

- [25] A. C. Shi, M. F. Tang, and Q. J. Zhou, "Research of deformation characteristics of columnar jointed basalt at baihetan hydropower station on Jinsha river," *Chinese Journal of Rock Mechanics and Engineering*, vol. 27, no. 10, pp. 2079–2086, 2008, in Chinese.
- [26] C. S. Zhang, X. R. Chen, J. Hou et al., "Study of mechanical behavior of deep-buried marble at Jinping II hydropower station," *Chinese Journal of Rock Mechanics and Engineering*, vol. 29, no. 10, pp. 1999–2009, 2010, in Chinese.
- [27] L. Chen, S. Bai, and X. Yin, "Physical simulation on failure around a circular cavern in hard and brittle rock under high and increasing natural stress conditions," *Journal of Engineering Mechanics*, vol. 140, no. 2, pp. 332–344, 2014.
- [28] X. B. Zhao, J. Zhao, and J. G. Cai, "P-wave transmission across fractures with nonlinear deformational behaviour," *International Journal for Numerical & Analytical Methods in Geomechanics*, vol. 30, no. 11, pp. 1097–1112, 2006.
- [29] C. H. Dowding, *Construction Vibration*, Prentice-Hall, Upper Saddle River, NY, USA, 1996.
- [30] J. B. Walsh, "Seismic wave attenuation in rock due to friction," *Journal of Geophysical Research*, vol. 71, no. 10, pp. 2591–2599, 1966.